


NANO EXPRESS

Open Access



# Quick Optical Identification of the Defect Formation in Monolayer WSe<sub>2</sub> for Growth Optimization

Long Fang<sup>1</sup>, Haitao Chen<sup>2</sup>, Xiaoming Yuan<sup>1\*</sup> , Han Huang<sup>1</sup>, Gen Chen<sup>3</sup>, Lin Li<sup>1</sup>, Junnan Ding<sup>1</sup>, Jun He<sup>1</sup> and Shaohua Tao<sup>1\*</sup>

## Abstract

Bottom-up epitaxy has been widely applied for transition metal dichalcogenides (TMDCs) growth. However, this method usually leads to a high density of defects in the crystal, which limits its optoelectronic performance. Here, we show the effect of growth temperature on the defect formation, optical performance, and crystal stability in monolayer WSe<sub>2</sub> via a combination of Raman and photoluminescence (PL) spectroscopy study. We found that the defect formation and distribution in monolayer WSe<sub>2</sub> are closely related to the growth temperature. These defect density and distribution can be controlled by adjusting the growth temperature. Aging experiments directly demonstrate that these defects are an active center for the decomposition process. Instead, monolayer WSe<sub>2</sub> grown under optimal conditions shows a strong and uniform emission dominated by neutral exciton at room temperature. The results provide an effective approach to optimize TMDCs growth.

**Keywords:** WSe<sub>2</sub>, Defects, Crystal stability, Photoluminescence, Raman scattering

## Introduction

Ultrathin TMDCs (MX<sub>2</sub>, M = Mo, W; X = Se, S, etc.) have been widely applied in the photonic and optoelectronic application fields, such as photodetectors [1–4], ultrathin transistors [5, 6], photovoltaic devices [7, 8], sensors [9, 10], and electrocatalysis [11]. Compared with mechanical exfoliation method, chemical vapor deposition (CVD) shows great advantages in massive production, morphology, and structure controlling [12–15], which are highly desired for large-area flexible material development and optoelectronic device applications [2, 16–18]. However, the formation of lattice defects in two-dimensional (2D) materials during the CVD growth is detrimental to its photoelectric properties, device performance, and even the crystal stability. For example, the hole mobility of WSe<sub>2</sub> field-effect transistor fabricated using CVD grown monolayer is far below the theoretical predictions [19]. The defect formation-induced nonuniform photoluminescence (PL) emission distribution has been

widely observed in the grown TMDCs monolayer [20–24]. CVD-grown TMDCs monolayer shows poor lattice stability in the air [25]. The high defect density in CVD-grown 2D materials significantly limits their device performance and stability, especially for devices exposed to the air for a long time.

The most direct and effective methods for 2D materials defect detection are transmission electron microscopy (TEM) [26] and scanning tunneling microscopy (STM) technique [27]. But these methods usually require sample transferring which could cause new defects. In addition, these methods are time-consuming and only detect the defects in a small area. For the growth optimization, a quick and nondestructive evaluation method is highly demanded. Raman spectroscopy is an important and nondestructive method to probe the lattice vibration, lattice distortion, and electronic properties of materials [28, 29]. For instance, the XeF<sub>2</sub> treatment-induced defects in WSe<sub>2</sub> have been studied by comparing the E<sub>12g</sub> peak intensity, the peak shift, and the full width at half maximum (FWHM) [30]. PL spectroscopy shows advantages in quickly determining the optical properties and detecting the electronic structure TMDCs

\* Correspondence: [xiaoming.yuan@csu.edu.cn](mailto:xiaoming.yuan@csu.edu.cn); [eshtao@csu.edu.cn](mailto:eshtao@csu.edu.cn)

<sup>1</sup>Hunan Key Laboratory of Super Micro-structure and Ultrafast Process, School of Physics and Electronics, Central South University, Changsha 410083, China  
Full list of author information is available at the end of the article

without damaging. So it is widely used to study the optical properties of TMDCs [2, 31, 32]. In addition, PL is quite sensitive to the excitons, trions, and defects in monolayer TMDCs [33–36]. Rosenberger et al. show an inverse relationship between the PL intensity of monolayer  $\text{WS}_2$  and defect density [21]. Further research shows that the weak PL is mostly due to the formation of negatively charged excitons [37]. Therefore, optical characterization offers a quick and nondestructive method to evaluate the localized defects and crystal quality of TMDCs.

Growth time and growth temperature are the two most important parameters affecting the growth of 2D materials. These effects on the growth duration of CVD-grown  $\text{WSe}_2$  monolayer have been reported before [38]. Therefore, in this work, we try to focus on the optical property difference of  $\text{WSe}_2$  grown at different temperatures and study the defect-induced crystal stability differences. The optical performance and the lattice quality are examined using confocal Raman and PL techniques for growth optimization. The crystal defects are found to weaken the PL emission intensity and lead to a nonuniform emission distribution in the triangle  $\text{WSe}_2$  domain due to defect density difference. Moreover, these defects cause a low energy emission peak in the PL spectrum, as observed in both room temperature and low-temperature PL spectra. In addition to the negative effect on the optical performance, the defects deteriorate the crystal stability in the air, resulting in faster decomposition rate of  $\text{WSe}_2$ . Based on the optical characterization results, we found that there exists an optimal growth temperature for  $\text{WSe}_2$ . In our case, this temperature is 920 °C. Either reducing or increasing the growth temperature impacts the optical properties and crystal stability of monolayer  $\text{WSe}_2$ . These results provide an approach for us to optimize the optical properties and crystal stability of 2D materials [39].

## Methods

### Synthesis of Monolayer $\text{WSe}_2$

Monolayer  $\text{WSe}_2$  was synthesized using high-purity Se powder (Alfa-Aesar 99.999%) and  $\text{WO}_3$  powder (Aladdin 99.99%) using a 2-inch-diameter quartz tube furnace. The Se powders (30 mg) were placed in a quartz boat at the first heating zone.  $\text{WO}_3$  powders (100 mg) were placed in a quartz boat at the second heating zone. The distance between the Se powder and  $\text{WO}_3$  powder is about 25 cm. *c*-plane (0001) sapphire substrates were cleaned and placed at downstream (5~10 cm) of the  $\text{WO}_3$  solid sources. Before the experiments, the chamber was pumped about 10 min and flushed with high-purity Ar carrier gas (99.9999 %) under a flow of 200 standard-state cubic centimeter per minute (sccm) at room temperature to remove the oxygen contamination. After

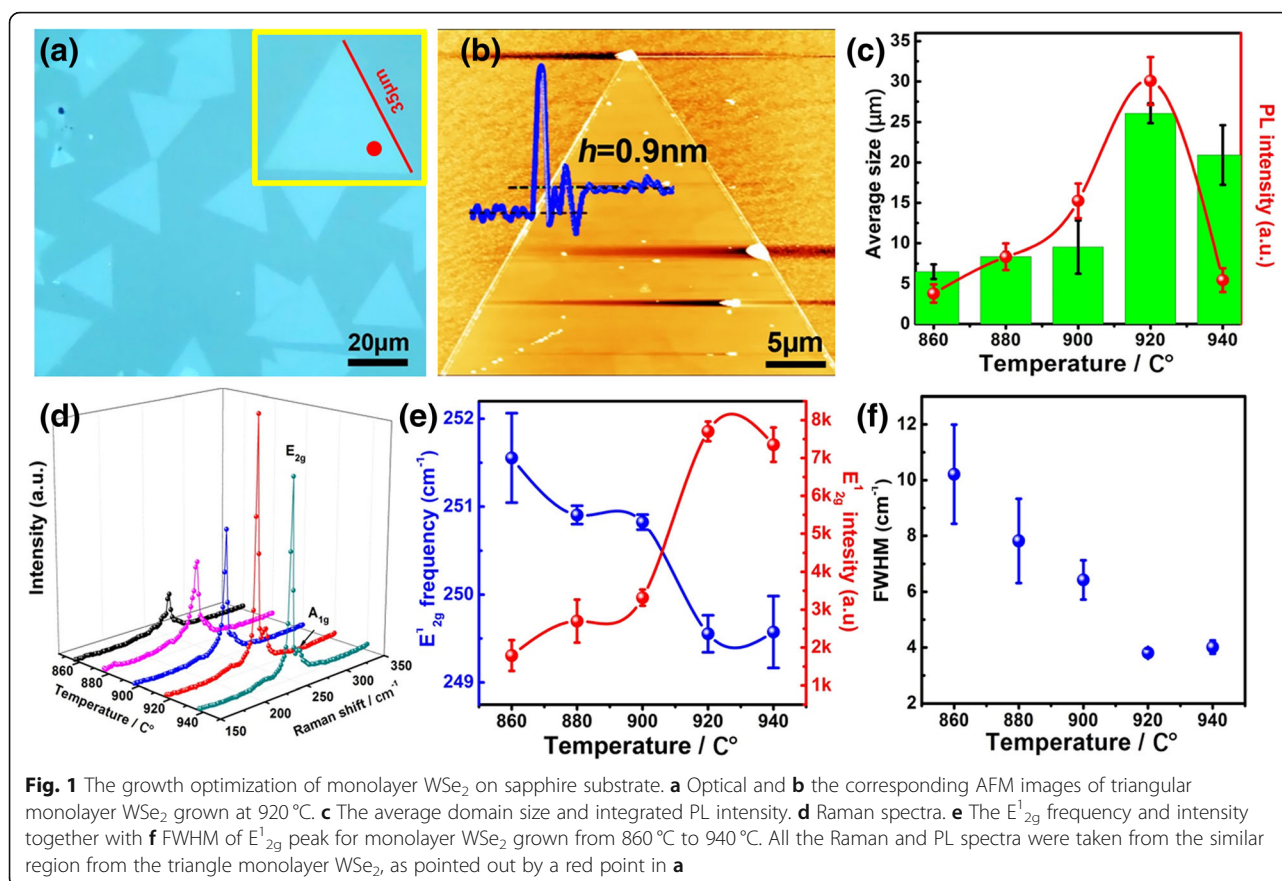
that, 10%  $\text{H}_2$  and Ar mixture gas with a flow of 50 sccm was introduced into the furnace at an ambient pressure. The second heating zone was heated to the target temperature (860~940 °C) at a ramping rate of 20 °C/min. After that, the temperature was maintained at the growth temperature for 6 min. Meanwhile, the first heating zone was kept at 320 °C. After growth, the furnace was cooled to room temperature.

### Characterization

The morphology of as-grown  $\text{WSe}_2$  was examined using an optical microscopy (NPLANEPi100X). Raman scattering and micro-PL measurements were performed using a Renishaw system (inVia Qontor). The excitation was pumped through an objective lens ( $\times 100$ ) with a green (532 nm) laser and 1800 lines/mm grating. Atomic force microscope (AFM) measurements were performed using an Agilent system (Agilent 5500, Digital Instruments, tapping mode). The morphology changes of monolayer  $\text{WSe}_2$  were examined by scanning electron microscopy (SEM, TESCAN MIRA3 LMU).

## Results and Discussion

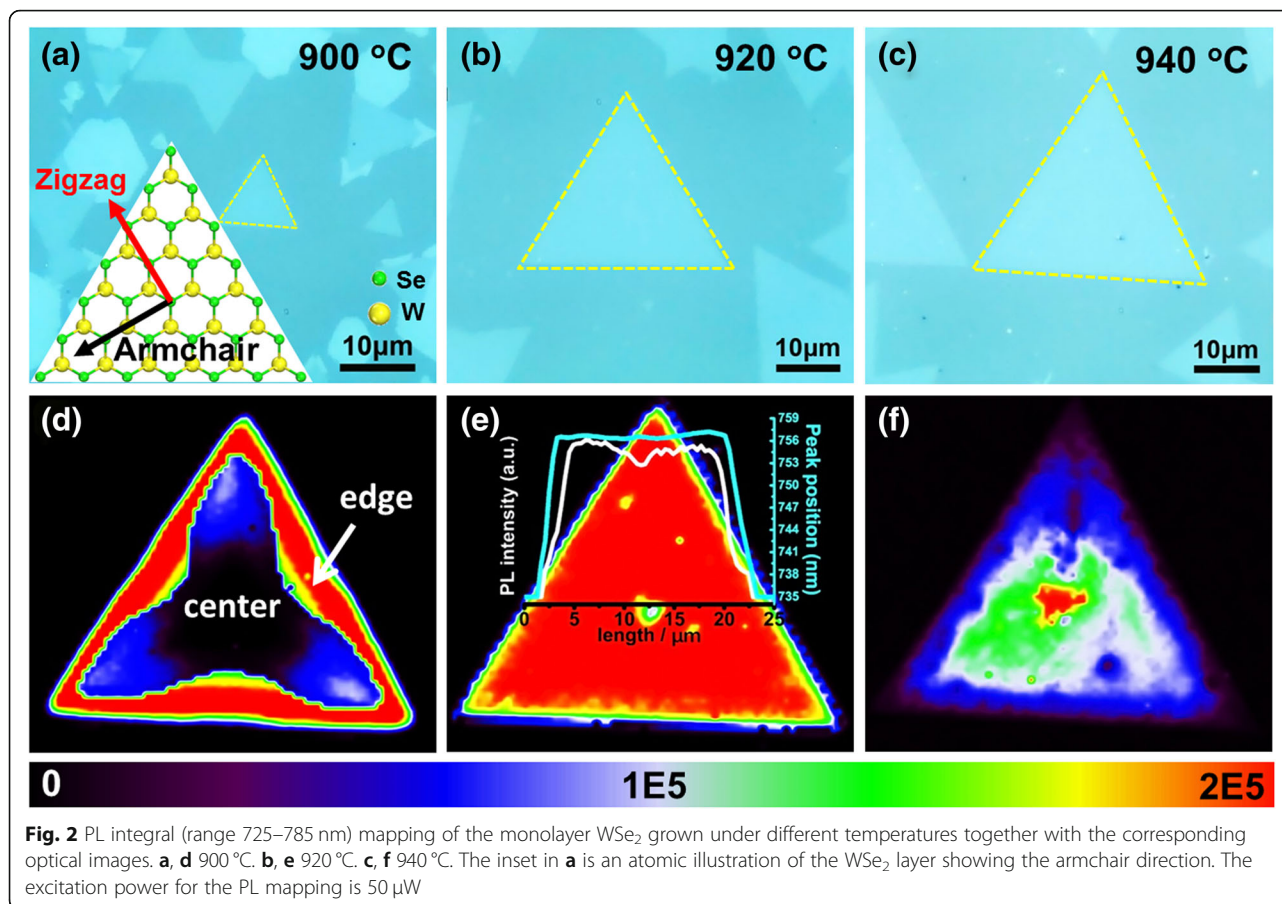
The effect of growth temperature on the  $\text{WSe}_2$  was performed during the temperature range from 860 to 940 °C. Statistical analysis of optical microscopy images and PL performance indicates that the optimal growth temperature is 920 °C, as demonstrated in Fig. 1a, c. Furthermore, at 920 °C, the effect of growth time on the sizes and density of CVD-grown  $\text{WSe}_2$  flakes has been studied. The size of  $\text{WSe}_2$  flakes gradually increases with time (3–20 min), and the obtained results are quite similar to those published before [38]. When the growth time is 20 min, even a millimeter-scale  $\text{WSe}_2$  film can be grown. After film formation, a second layer is formed (more optical microscopy images and PL statistics are shown in Additional file 1: Figure S1–S3 in the supporting information (SI)). Under the 920 °C, a high density of triangular  $\text{WSe}_2$  domain with uniform size is formed with an average edge length of  $\sim 35 \mu\text{m}$ . AFM characterization shows a thickness of  $\sim 0.9 \text{ nm}$  (see Fig. 1b). Furthermore, the Raman scattering detects the characteristic vibration modes ( $E_{2g}^1$  and  $A_{1g}$ ) of  $\text{WSe}_2$  to be at  $\sim 249.5$  and  $\sim 260 \text{ cm}^{-1}$ , respectively (see Fig. 1d), which have also been observed in previous reports [38, 40]. No  $B_{2g}$  ( $308 \text{ cm}^{-1}$ ) mode which represents the vibration between different layers is detected [30, 41]. These results indicate that the as-grown  $\text{WSe}_2$  is monolayer. Lowering or increasing the growth temperature leads to a drop of both the density and size of  $\text{WSe}_2$  domains. At low growth temperature (860 °C), the density of  $\text{WSe}_2$  is much lower and the grain size is reduced to  $\sim 5 \mu\text{m}$ . Improving the growth temperature to 920 °C increases the nucleation density and the crystal growth speed (see Fig. 1c) [42]. The



domain size drops again as the temperature exceeds 920 °C, which is probably due to a higher decomposition velocity. Despite the morphology difference, the grown WSe<sub>2</sub> during the investigated temperature range (860 to 940 °C) are all monolayer. The photon emission intensity and the domain size evolution trend with temperature are quite similar, posing the strongest PL emission intensity at 920 °C (see Fig. 1c). This emission intensity difference suggests that even though monolayer WSe<sub>2</sub> can be obtained under different growth temperatures, however, their optical performance varies drastically. The reason for this PL emission difference can be revealed by the Raman scattering as well. Figure 1d compares the Raman spectra of WSe<sub>2</sub> at different growth temperature, from 860 to 940 °C (more Raman spectroscopy statistics are shown in Additional file 1: Figure S4). The absence of B<sub>2g</sub> mode indicates that WSe<sub>2</sub> is monolayer grown at different temperatures [30, 41]. The E<sub>12g</sub><sup>1</sup> frequency and intensity are related to the strain level and crystal quality [23, 43, 44], and the FWHM of the Raman peak can reflect the 2D materials crystal quality. The narrower FWHM indicates a higher crystal quality of the 2D materials [12]. Both experiments and theoretical calculations demonstrate that E<sub>12g</sub><sup>1</sup> peaks around 249.5 cm<sup>-1</sup> for ideal WSe<sub>2</sub> monolayer crystal [41, 45]. Figure 1e shows the E<sub>12g</sub><sup>1</sup> frequency and intensity as a function

of temperature. The E<sub>12g</sub><sup>1</sup> frequency drops from 251.5 cm<sup>-1</sup> to a minimum of 249.5 cm<sup>-1</sup> at 920 °C before increases again during the investigated temperature range, and the FWHM shows a similar trend as the E<sub>12g</sub><sup>1</sup> frequency (see Fig. 1f). In addition, the E<sub>12g</sub><sup>1</sup> peak intensity poses a maximum intensity at 920 °C. Considering the highest Raman scattering intensity, the narrowest FWHM, the perfect matched Raman peak (the E<sub>12g</sub><sup>1</sup> peak is around 249.5 cm<sup>-1</sup> for ideal monolayer WSe<sub>2</sub>), and the strongest PL emission intensity, we demonstrate that monolayer WSe<sub>2</sub> grown at 920 °C shows the purist crystal quality [12, 30].

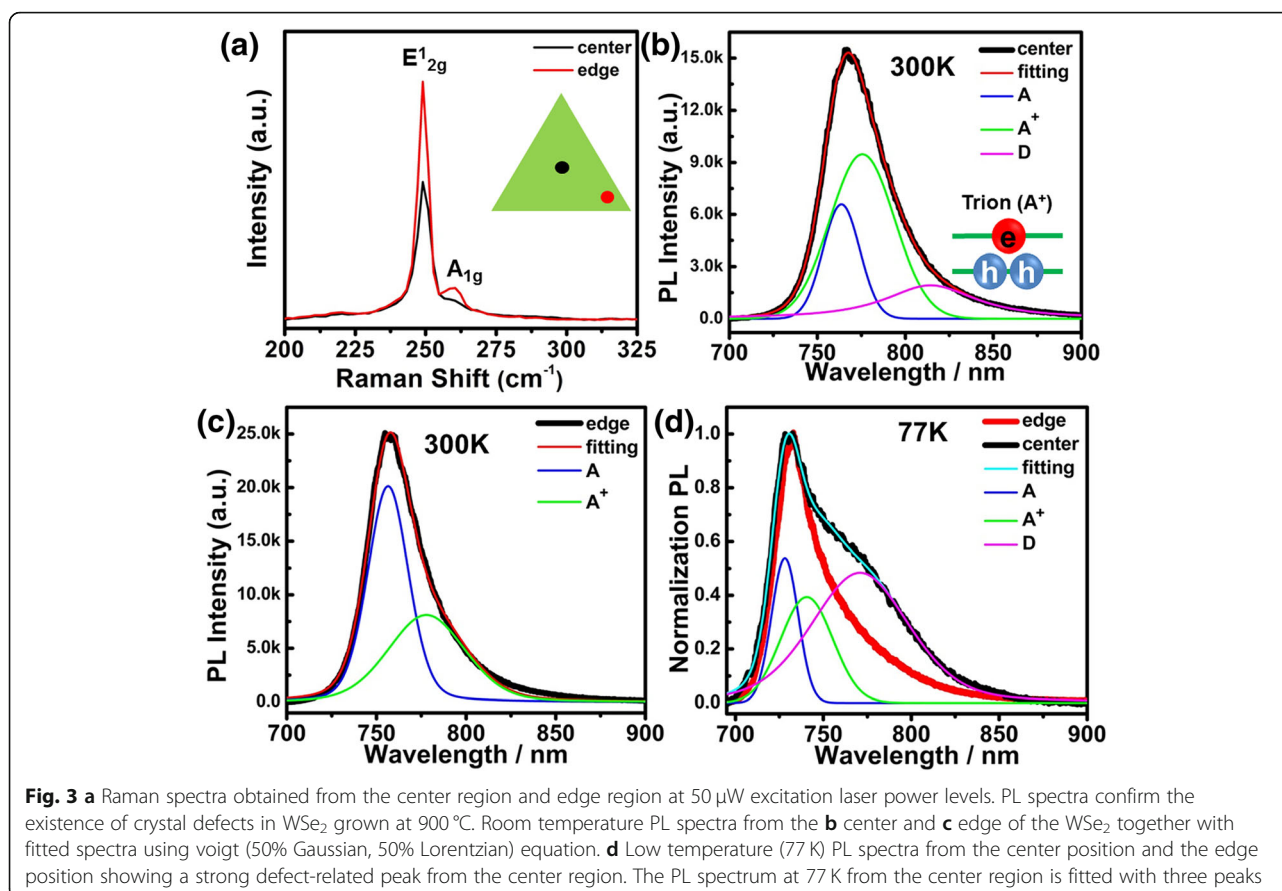
The emission intensity uniformity of the grown WSe<sub>2</sub> monolayer is examined by PL mapping, as compared in Fig. 2, showing a temperature-dependent emission intensity distribution. The photon emission of WSe<sub>2</sub> layer grown at 920 °C distributes uniformly for the entire monolayer except for the center region where WO<sub>3-x</sub> and WO<sub>3-x</sub>Se<sub>y</sub> are formed under Se-deficient atmosphere as a nucleation center for the continued WSe<sub>2</sub> growth [46–48]. The inset PL intensity line scanning results further confirm the constant emission intensity and the emission energy. However, the PL emission intensity turns to inhomogeneous for other growth temperatures (see Fig. 2d–f). For lower growth temperature (900 °C), the emission intensity from the inner concave triangle



region is much weaker than those close to the triangle edge. According to the WSe<sub>2</sub> atom arrangement in a triangle domain [49, 50], the weak emission is along the armchair direction. Under a higher growth temperature (940 °C, see Fig. 2f), the PL intensity map poses another intensity pattern. The strongest PL intensity occurs at the center area and progressively decreases to the triangle edge (see more examples in Additional file 1: Figure S5). This emission difference cannot be observed by optical or AFM measurements. PL emission in monolayer TMDCs crystal is usually nonuniform and has been observed quite a few times in both CVD-grown [21–23, 51–53] and mechanically exfoliated layers [24, 54–56]. The main causes of nonuniform PL emission include lattice defects (including impurities [56, 57] and vacancies [27]), localized electronic states [52, 58], strain [43], and edge effect [22]. In our experiment, no similar feature due to localized electronic states or edge effect is observed. The strain should not be the main factor causing the distribution of PL intensity due to the following reasons. First, for WSe<sub>2</sub> grown at 900 °C, the center and the edge regions undergo the same heat treatment; the resulted strain level should be the same [59]. Secondly, Kim et al. compared the PL of WS<sub>2</sub> before and after

transferring to transmission electron microscopy (TEM) copper grid, excluding the possibility of the substrate caused nonuniform PL and Raman distribution [58]. Thirdly, the E<sup>1</sup><sub>2g</sub> mode is sensitive to the strain and is used to estimate the strain level [44]. The E<sup>1</sup><sub>2g</sub> peak of center and edge region in monolayer WSe<sub>2</sub> growth at 900 °C is the same (249 cm<sup>-1</sup>) without any sign of peak shift (as shown in Fig. 3a), indicating a nearly constant strain level distribution between the substrate and WSe<sub>2</sub>. According to the above discussions, we speculate that the emission inhomogeneous is a reflection of the defect density distribution. The emission intensity from the bright emission region of samples grown at different temperatures is quite similar, indicating a similar crystal quality in these regions despite the growth temperature difference.

The Raman and PL emission spectra from the center and edge of monolayer WSe<sub>2</sub> grown at 900 °C are compared in Fig. 3. The obtained PL spectra from center position is deconvoluted into three peaks: neutral exciton at ~1.624 eV (marked as A) [51, 52], trion at 1.60 eV (marked as A<sup>+</sup>) [29, 52], and an unknown emission peak (marked as D) around 1.53 eV (the detailed fitting basis are shown in Additional file 1: Figures S6–S8). Figure 3b shows the PL emission is dominated by the A<sup>+</sup>



in the center position. The binding energy for  $A^+$  is estimated to be about 24 meV, which is the energy difference between trions and neutral exciton [36]. It fits perfectly with the value of positive trion in the literature [33, 35], where the trion consists of two holes ( $h^+$ ) and an electron ( $e^-$ ). Indeed, recent studies reveal that CVD-grown  $\text{WSe}_2$  is usually p-type due to the formation of tungsten vacancy [27]. These results are consistent with the general rules of doping effects in semiconductors. During the power-dependent PL experiments, D emission quickly saturates (see Additional file 1: Figure S7 in the SI), suggesting that the unknown emission is actually caused by the lattice defects, as observed in other reports [24, 33, 51, 52]. In comparison, the emission from the edge does not contain this defect-related peak. Instead, the emission peak is much narrower and stronger, consisting of mainly neutral exciton peak with trion peak as a shoulder. During the power-dependent PL experiments, the FWHM of  $\text{WSe}_2$  on both center and edge does not change with power, indicating no signs of local heating effect (see Additional file 1: Figure S8 in the SI) [51, 60]. This defect-related emission peak becomes more obvious at low temperature (77 K), as compared in Fig. 3d. The PL spectrum at 77 K from the center region consists of three emission peaks. Through calculations,

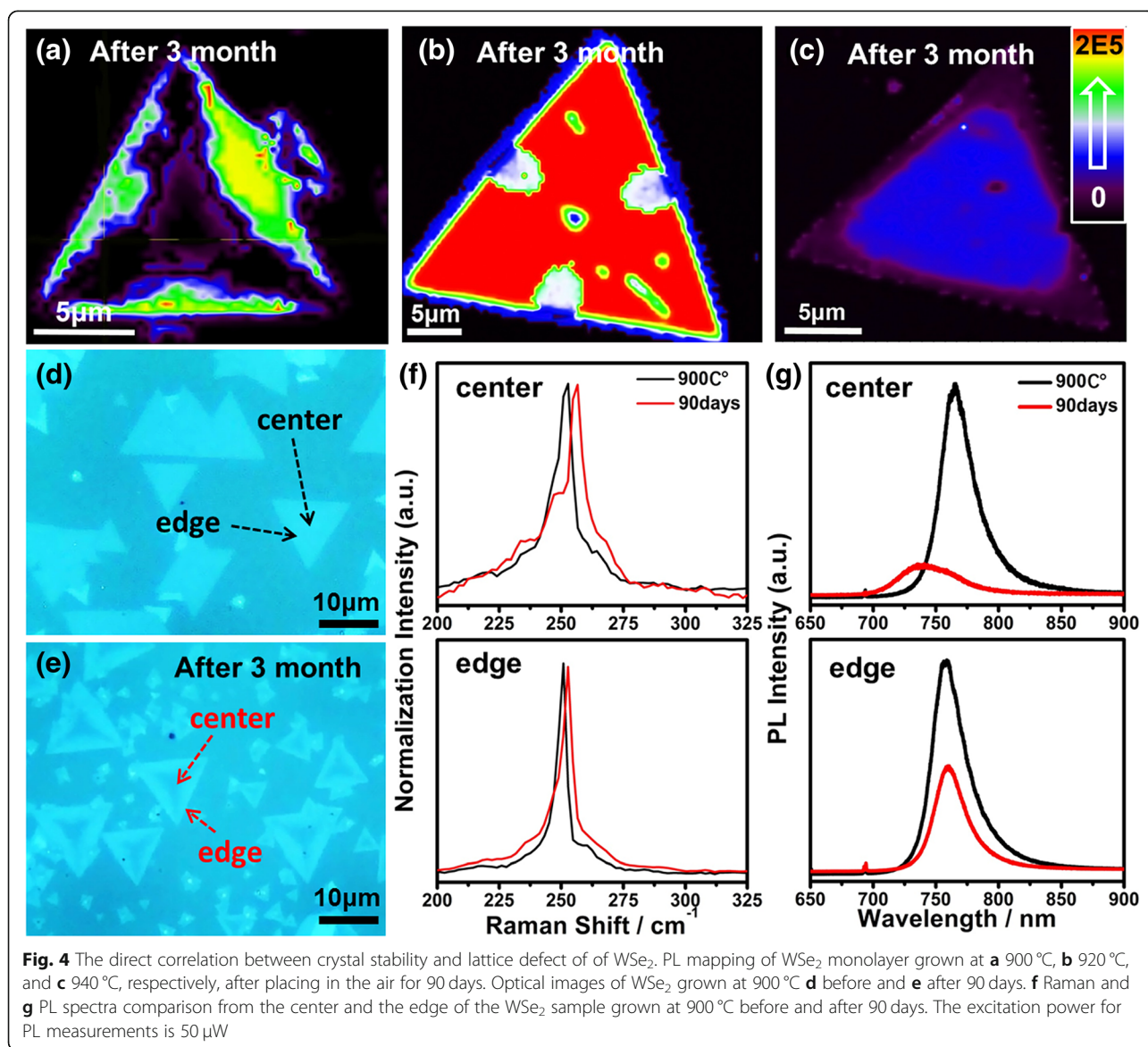
the binding energies of monolayer  $\text{WSe}_2$  for trion ( $A^+$ ) and defect-related emission are around 24 meV and 100 meV, respectively, which are consistent with our room temperature PL fitting results.

These results confirm the existence of the crystal defect in the CVD-grown  $\text{WSe}_2$  monolayer. These defects are centers for nonradioactive recombination, thus dropping the photon emission efficiency [24, 61]. Moreover, the defect density is position and growth condition dependent, leading to different emission distribution pattern in Fig. 2. Under poor growth conditions, monolayer  $\text{WSe}_2$  can still form. However, a large proportion of area is highly defected and contains only a small area with high crystal purity. PL spectrum and mapping provide a quick method to evaluate its crystal quality and guide the growth optimization. According to the above analysis, the monolayer  $\text{WSe}_2$  growth at lower growth temperature shows a weaker crystal quality, which could be due to insufficient reaction between the  $\text{WO}_{3-x}$  and Se gas [62, 63]. Improving the temperature could thus overcome the reaction barrier and form  $\text{WSe}_2$  with high crystal quality (920  $^\circ\text{C}$ ). However, keeping increasing the temperature (940  $^\circ\text{C}$ ) could lead to the decomposition of the formed monolayer  $\text{WSe}_2$  under insufficient Se gas protection [64]. Thus, the defect formation mechanism

could vary at different growth temperatures, thereby leading to different emission distribution patterns. We found that the PL intensity of inner region of the triangle is the lowest. The decrease of PL intensity suggests that the crystal defects of the  $\text{WSe}_2$  were produced from the center of the triangle, which is consistent with previous reports [51]. In addition, the probability of lattice distortion along the armchair (see Fig. 2a) direction is larger for monolayer  $\text{WSe}_2$  at  $900^\circ\text{C}$ . As the  $\text{WSe}_2$  grown from the center of the triangle to the three angle edges of the triangle, the crystal quality of  $\text{WSe}_2$  is getting better.

Crystal stability is always an issue for the monolayer TMDCs crystal, and the existence of crystal defect usually makes this situation even worse. A direct relationship between the crystal defects and the decomposition

of  $\text{WSe}_2$  is revealed in Fig. 4. After keeping the measured samples in air conditions for another 90 days, the PL emission intensity for samples grown under  $900^\circ\text{C}$  and  $940^\circ\text{C}$  are remarkably decreased as expected due to quick decomposition while the emission intensity distribution pattern does not change drastically. This crystal deterioration can even be observed using optical microscopy, as shown in Fig. 4d, e. The decomposed region matches perfectly with the low PL emission region in Fig. 2d. This observation suggests that the formed defects in  $\text{WSe}_2$  act as a center for the decomposition process, largely reducing the crystal stability in air. In contrast,  $\text{WSe}_2$  grown at optimal temperature with the purist crystal quality presents a much better crystal stability. The emission intensity drop is not obvious and still shows a strong PL emission. However, the emission



intensity becomes inhomogeneous with weak emission at the center of the triangle edge (see more examples in Additional file 1: Figure S5). This suggests that the decomposition or crystal deterioration process in high-quality WSe<sub>2</sub> begins from the center of the triangle edge. The PL and Raman spectra of WSe<sub>2</sub> grown at 900 °C before and after 90 days are compared in Fig. 4f, g. The E<sup>1</sup><sub>2g</sub> vibration mode of the center region is red-shifted by ~3.7 cm<sup>-1</sup> while this shift is only ~1.9 cm<sup>-1</sup> at the edge region. As discussed in Fig. 1, the results show that the crystal quality deteriorates faster in the region with a higher density of lattice defects. The existence of lattice defects would lower the energy barrier for WSe<sub>2</sub> decomposition and accelerate the decomposition process. The region with a higher defect density can easily combine with O and OH, deteriorating its lattice stability [25]. This process then gradually propagates throughout the entire monolayer WSe<sub>2</sub>. This lattice evolution process matches perfectly with our aging experiment processes (see Figs. 4e and 5). Consequently, WSe<sub>2</sub> grown at 900 °C starts to decompose from the center region. In comparison, WSe<sub>2</sub> grown at 920 °C decomposes more slowly due to a better crystal quality. And the decomposition initiates from the more chemically active regions, such as edges and grain boundaries [65], as has been demonstrated in Fig. 4b.

The PL emission in Fig. 4g shows a similar trend. Compared with the data measured 90 days before, the PL peak position and emission intensity of the center region are blue-shifted by ~60 meV and decreased 7 times,

respectively. Moreover, the FWHM is broadened by ~17 meV. In contrast, the PL peak position and FWHM of the edge are nearly the same and the emission intensity only drops to half of the intensity measured at 90 days before. Using the same approach, we found that the crystal deterioration process in monolayer WSe<sub>2</sub> grown at 940 °C shows the same mechanism: the higher the crystal quality, the slower is the decomposition.

In order to better understand the aging process, the morphology evolution of monolayer WSe<sub>2</sub> grown at 900 °C with time is shown in Fig. 5. The aged region starts from the center of the triangle (see Fig. 5b). As the aging time increases, WSe<sub>2</sub> decomposes gradually from the center to the vertex of the triangle as shown in Fig. 5c. After 180 days, WSe<sub>2</sub> at the center of the triangle and the three angular positions have been substantially decomposed completely. At this time, the PL in the center and triangle has quenched. Raman scattering in these decomposed areas shows no signal of vibration mode of WSe<sub>2</sub>, confirming the complete decomposition of WSe<sub>2</sub> crystal. The aging study of a single layer of WSe<sub>2</sub> grown at 900 °C further demonstrates that the location of the decomposition agrees very well with our previously measured PL mapping results. According to the above discussions, the critical factor affecting the stability of WSe<sub>2</sub> is the unwanted defect formation during the CVD growth. PL and Raman spectrum provides an easy approach to quickly examine the crystal quality to guide the growth optimization towards 2D layer with the purest crystal quality.

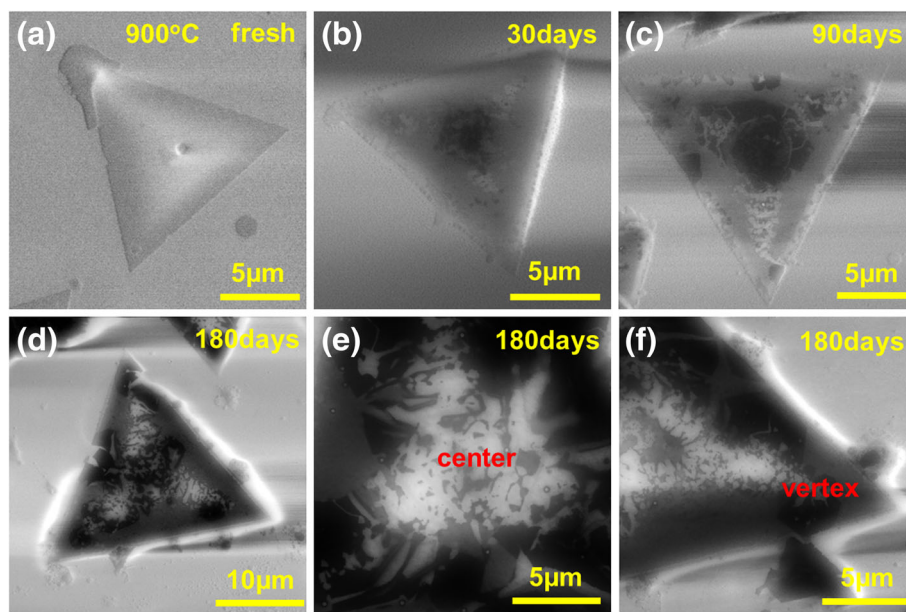


**Fig. 5** SEM images of **a** fresh monolayer WSe<sub>2</sub> grown at 900 °C, placing in the air for **b** 30 days, **c** 90 days, and **d** 180 days, respectively. The enlarged view of the center and angle **f** in **d**. All the samples were stored in 25 °C. **e**, **f** Enlarged views of the center and vertex of monolayer **d**, respectively

## Conclusion

In summary, we study the role of growth temperature on crystal defect formation and crystal stability of monolayer  $\text{WSe}_2$  on a sapphire substrate. PL and Raman spectroscopy techniques are applied to quickly identify the crystal quality, stability, and defect distribution of as-grown monolayer  $\text{WSe}_2$  at different conditions. Through this characterization approach, the optimal growth temperature for monolayer  $\text{WSe}_2$  is obtained at 920 °C. Either reducing or increasing the growth temperature leads to the formation of a higher defect density. At lower growth temperature, the defect formation is probably due to the unfully decomposed  $\text{WO}_{3-x}$  precursor. The defects start to form at the nucleus center and then proceed along the armchair direction of the crystal, forming an inner triangular shape with a high density of defects and lower PL emission intensity. Above the optimal growth temperature, the defect distribution shows another pattern and starts from the edge, probably due to the decomposition of  $\text{WSe}_2$  at such a high temperature. PL emission shows that photon emission in the defected region is dominated by trions while neutral exciton emission is prominent in the  $\text{WSe}_2$  monolayer with better crystal quality. The aging experiment further proved that the region with a higher defect density can easily combine with O and OH, deteriorating its lattice stability. These results offer insights into the optimum synthesis of various 2D materials and the potential applications in the field of optoelectronics.

## Additional file

**Additional file 1: Figure S1.** More optical images of  $\text{WSe}_2$  samples grown on sapphire substrates: (a) 860 °C, (b) 880 °C, (c) 900 °C, (d) 920 °C and (e) 940 °C. **Figure S2.** Optical microscopy images of  $\text{WSe}_2$  grown for (a) 4 min, (b) 7 min, (c) 10 min and (d) 20 min. The growth temperatures are 920 °C for all cases. **Figure S3.** Raman spectra of five different monolayer  $\text{WSe}_2$  samples grown at (a) 860 °C, (b) 880 °C, (c) 900 °C, (d) 920 °C and (e) 940 °C, respectively. **Figure S4.** Raman spectra of 5 different monolayer  $\text{WSe}_2$  samples grown at (a) 860 °C, (b) 880 °C, (c) 900 °C, (d) 920 °C and (e) 940 °C, respectively. **Figure S5.** More PL integral intensity mapping of  $\text{WSe}_2$  monolayer: (a) 900 °C, (b) 920 °C and (c) 940 °C, respectively. (d) PL intensity mapping of  $\text{WSe}_2$  grown at 920 °C after placing in the air for another 90 days. **Figure S6.** Deconvoluted spectra obtained with excitation laser power levels of 5  $\mu\text{W}$ , 10  $\mu\text{W}$ , 50  $\mu\text{W}$ , 100  $\mu\text{W}$  and 500  $\mu\text{W}$ , respectively, corresponding to the positions in the center region. **Figure S7.** Deconvoluted spectra obtained with excitation laser power levels of 5  $\mu\text{W}$ , 10  $\mu\text{W}$ , 50  $\mu\text{W}$ , 100  $\mu\text{W}$  and 500  $\mu\text{W}$ , respectively, corresponding to the positions in the edge region. **Figure S8.** The deconvoluted PL peak position (a) and FWHM (b) of neutral exciton (A), trion ( $\text{A}^+$ ), and defects (D) as a function of laser power at the center and edge regions, respectively. The excitation power is 50  $\mu\text{W}$ . (DOCX 5032 kb)

## Abbreviations

2D: two-dimensional; AFM: Atomic force microscope; CVD: Chemical vapor deposition; FWHM: Full width at half maximum; PL: Photoluminescence; sccm: standard-state cubic centimeter per minute; SEM: Scanning electron microscope; STM: Scanning tunneling microscopy; TEM: Transmission electron microscopy; TMDCs: Transition metal dichalcogenides

## Acknowledgements

We thank the Analytical and Testing of Hunan Key Laboratory of Super Micro-structure and Ultrafast Process, School of Physics and Electronics, Central South University, as well as School of Materials Science and Engineering, Central South University.

## Authors' Contributions

ST, XY, and LF conceived the idea of experiments. LF, LL, and JD carried out the experiments. ST, XY, HC, HH, GC, and JH participated in the discussion and analysis of the experimental result. LF and XY co-wrote this paper. ST, XY, and HC modified the manuscript. All authors read and approved the final manuscript.

## Funding

This work is supported by the National Natural Science Foundation of China (No.51702368, No.11674401, and No.11804387), the Hunan Provincial Natural Science Foundation of China (2018JJ3684), the Innovation-Driven Project of Central South University (2018CX045), the Fundamental Research Funds for the Central South University (No. 1053320181264), the Independent Exploration and Innovation Project for Postgraduates of Central South University (2018tztz103), and the Open-End Fund for the Valuable and Precision Instruments of Central South University (CSUZC201826).

## Availability of Data and Materials

All data are fully available without restriction.

## Competing Interests

The authors declare that they have no competing interests.

## Author details

<sup>1</sup>Hunan Key Laboratory of Super Micro-structure and Ultrafast Process, School of Physics and Electronics, Central South University, Changsha 410083, China. <sup>2</sup>College of Advanced Interdisciplinary Studies, National University of Defense Technology, Changsha 410083, China. <sup>3</sup>School of Materials Science and Engineering, Central South University, Changsha 410083, China.

Received: 5 June 2019 Accepted: 29 July 2019

Published online: 14 August 2019

## References

- Miao JS, Hu WD, Jing YL, Luo WJ, Liao L, Pan AL, Wu SW, Cheng JX, Chen XS, Lu W (2015) Surface plasmon-enhanced photodetection in few layer  $\text{MoS}_2$  phototransistors with Au nanostructure arrays. *Small* 11(20):2392–2398
- Lan C, Zhou Z, Zhou Z, Li C, Shu L, Shen L, Li D, Dong R, Yip S, Ho JC (2018) Wafer-scale synthesis of monolayer  $\text{WS}_2$  for high-performance flexible photodetectors by enhanced chemical vapor deposition. *Nano Res* 11(6):3371–3384
- Yang W, Chen J, Zhang Y, Zhang Y, He JH, Fang X (2019) Silicon-compatible photodetectors: trends to monolithically integrate photosensors with chip technology. *Adv Funct Mater* 29:1808182
- Xu H, Han XY, Dai X, Liu W, Wu J, Zhu JT, Kim DY, Zou GF, Sablon KA, Sergeev A, Guo ZX, Liu HY (2018) High detectivity and transparent few-layer  $\text{MoS}_2$ /glassy-graphene heterostructure photodetectors. *Adv Mater* 30(13):1706561
- Radisavljevic B, Kis A (2013) Mobility engineering and a metal-insulator transition in monolayer  $\text{MoS}_2$ . *Nat Mater* 12(9):815–820
- Jiang J, Hu W, Xie D, Yang J, He J, Gao Y, Wan Q (2019) 2D electric-double-layer phototransistor for photoelectronic and spatiotemporal hybrid neuromorphic integration. *Nanoscale* 11(3):1360–1369
- Tsai ML, Su SH, Chang JK, Tsai DS, Chen CH, Wu CI, Li LJ, Chen LJ, He JH (2014) Monolayer  $\text{MoS}_2$  heterojunction solar cells. *ACS Nano* 8(8):8317–8322
- Zheng X, Wei Y, Liu J, Wang S, Shi J, Yang H, Peng G, Deng C, Luo W, Zhao Y, Li Y, Sun K, Wan W, Xie H, Gao Y, Zhang X, Huang H (2019) A homogeneous p-n junction diode by selective doping of few layer  $\text{MoSe}_2$  using ultraviolet ozone for high-performance photovoltaic devices. *Nanoscale* 11(28):13469–13476
- Medina H, Li JG, Su TY, Lan YW, Lee SH, Chen CW, Chen YZ, Manikandan A, Tsai SH, Navabi A, Zhu XD, Shih YC, Lin WS, Yang JH, Thomas SR, Wu BW, Shen CH, Shieh JM, Lin HN, Javey A, Wang KL, Chueh YL (2017) Wafer-scale growth of  $\text{WSe}_2$  monolayers toward phase-engineered hybrid  $\text{WO}_x/\text{WSe}_2$  films with sub-ppb  $\text{NO}_x$  gas sensing by a low-temperature plasma-assisted selenization process. *Chem Mat* 29(4):1587–1598



10. Ai YF, Hsu TH, Wu DC, Lee L, Chen JH, Chen YZ, Wu SC, Wu C, Wang ZMM, Chueh YL (2018) An ultrasensitive flexible pressure sensor for multimodal wearable electronic skins based on large-scale polystyrene ball@reduced graphene-oxide core-shell nanoparticles. *J Mater Chem C* 6(20):5514–5520
11. Alarawi A, Ramalingam V, He JH (2019) Recent advances in emerging single atom confined two-dimensional materials for water splitting applications. *Materials today energy* 11:1–23
12. Tian XL, Wei RF, Liu SS, Zhang YM, Qiu JR (2018) Photoluminescence nonuniformity from self-seeding nuclei in CVD-grown monolayer MoSe<sub>2</sub>. *Nanoscale* 10(2):752–757
13. Hao S, Yang BC, Gao YL (2016) Fracture-induced nanoscrolls from CVD-grown monolayer molybdenum disulfide. *Phys Status Solidi-Rapid Res Lett* 10(7):549–553
14. Xie QL, Zheng XM, Wu D, Chen XL, Shi J, Han XT, Zhang XA, Peng G, Gao YL, Huang H (2017) High electrical conductivity of individual epitaxially grown MoO<sub>2</sub> nanorods. *Appl Phys Lett* 111(9):093505
15. Wu D, Shi J, Zheng X, Liu J, Dou W, Gao Y, Yuan X, Ouyang F, Huang H (2019) CVD grown MoS<sub>2</sub> nanoribbons on MoS<sub>2</sub> covered sapphire (0001) without catalysts. *Phys Status Solidi-Rapid Res Lett* 13:1900063
16. Ji QQ, Zhang Y, Zhang YF, Liu ZF (2015) Chemical vapour deposition of group-VIB metal dichalcogenide monolayers: engineered substrates from amorphous to single crystalline. *Chemical Society Reviews* 44(9):2587–2602
17. Chen K, Wan X, Xu JB (2017) Epitaxial stitching and stacking growth of atomically thin transition-metal dichalcogenides (TMDCs) heterojunctions. *Adv Funct Mater* 27(19):1603884
18. Zhu JT, Xu H, Zou GF, Zhang W, Chai RQ, Choi J, Wu J, Liu HY, Shen GZ, Fan HY (2019) MoS<sub>2</sub>-OH bilayer-mediated growth of inch-sized monolayer MoS<sub>2</sub> on arbitrary substrates. *J Am Chem Soc* 141(13):5392–5401
19. Hong JH, Hu ZX, Probert M, Li K, Lv DH, Yang XN, Gu L, Mao NN, Feng QL, Xie LM, Zhang J, Wu DZ, Zhang ZY, Jin CH, Ji W, Zhang XX, Yuan J, Zhang Z (2015) Exploring atomic defects in molybdenum disulfide monolayers. *Nat Commun* 6:6293
20. Peimyo N, Shang JZ, Cong CX, Shen XN, Wu XY, Yeow EKL, Yu T (2013) Nonblinking, intense two-dimensional light emitter: monolayer WS<sub>2</sub> triangles. *ACS Nano* 7(12):10985–10994
21. Rosenberger MR, Chuang H-J, McCreary KM, Li CH, Jonker BT (2018) Electrical characterization of discrete defects and impact of defect density on photoluminescence in monolayer WS<sub>2</sub>. *ACS Nano* 12(2):1793–1800
22. Gutierrez HR, Perea-Lopez N, Elias AL, Berkdemir A, Wang B, Lv R, Lopez UF, Crespi VH, Terrones H, Terrones M (2013) Extraordinary room-temperature photoluminescence in triangular WS<sub>2</sub> monolayers. *Nano Lett* 13(8):3447–3454
23. Ye GL, Gong YJ, Lin JH, Li B, He YM, Pantelides ST, Zhou W, Vajtai R, Ajayan PM (2016) Defects engineered monolayer MoS<sub>2</sub> for improved hydrogen evolution reaction. *Nano Lett* 16(2):1097–1103
24. Wu Z, Luo Z, Shen Y, Zhao W, Wang W, Nan H, Guo X, Sun L, Wang X, You Y, Ni Z (2016) Defects as a factor limiting carrier mobility in WSe<sub>2</sub>: a spectroscopic investigation. *Nano Res* 9(12):3622–3631
25. Gao J, Li B, Tan J, Chow P, Lu TM, Koratkar N (2016) Aging of transition metal dichalcogenide monolayers. *ACS Nano* 10(2):2628–2635
26. Lin YC, Bjorkman T, Komsa HP, Teng PY, Yeh CH, Huang FS, Lin KH, Jadczyk J, Huang YS, Chiu PW, Krasheninnikov AV, Suenaga K (2015) Three-fold rotational defects in two-dimensional transition metal dichalcogenides. *Nat Commun* 6:6736
27. Zhang S, Wang CG, Li MY, Huang D, Li LJ, Ji W, Wu SW (2017) Defect structure of localized excitons in a WSe<sub>2</sub> monolayer. *Phys Rev Lett* 119(4):046101
28. Ferrari AC, Meyer JC, Scardaci V, Casiraghi C, Lazzeri M, Mauri F, Piscanec S, Jiang D, Novoselov KS, Roth S, Geim AK (2006) Raman spectrum of graphene and graphene layers. *Phys Rev Lett* 97(18):187401
29. Lu X, Luo X, Zhang J, Quek SY, Xiong QH (2016) Lattice vibrations and Raman scattering in two-dimensional layered materials beyond graphene. *Nano Res* 9(12):3559–3597
30. Zhang R, Drysdale D, Koutsos V, Cheung R (2017) Controlled layer thinning and p-type doping of WSe<sub>2</sub> by vapor XeF<sub>2</sub>. *Adv Funct Mater* 27(41):1702455
31. Alarawi A, Ramalingam V, Fu HC, Varadhan P, Yang R, He JH (2019) Enhanced photoelectrochemical hydrogen production efficiency of MoS<sub>2</sub>-Si heterojunction. *Opt Express* 27(8):A352–A363
32. Dong R, Lan C, Xu X, Liang X, Hu X, Li D, Zhou Z, Shu L, Yip S, Li C (2018) Novel series of quasi-2D Ruddlesden–Popper perovskites based on short-chained spacer cation for enhanced photodetection. *ACS Appl Mater Interfaces* 10(22):19019–19026
33. Jones AM, Yu HY, Ghimire NJ, Wu SF, Aivazian G, Ross JS, Zhao B, Yan JQ, Mandrus DG, Xiao D, Yao W, Xu XD (2013) Optical generation of excitonic valley coherence in monolayer WSe<sub>2</sub>. *Nat Nanotechnol* 8(9):634–638
34. You YM, Zhang XX, Berkelbach TC, Hybertsen MS, Reichman DR, Heinz TF (2015) Observation of biexcitons in monolayer WSe<sub>2</sub>. *Nat Phys* 11(6):477–481
35. Low T, Chaves A, Caldwell JD, Kumar A, Fang NX, Avouris P, Heinz TF, Guinea F, Martin-Moreno L, Koppens F (2017) Polaritons in layered two-dimensional materials. *Nat Mater* 16(2):182–194
36. Ross JS, Wu SF, Yu HY, Ghimire NJ, Jones AM, Aivazian G, Yan JQ, Mandrus DG, Xiao D, Yao W, Xu XD (2013) Electrical control of neutral and charged excitons in a monolayer semiconductor. *Nat Commun* 4:1474
37. Mak KF, He KL, Lee C, Lee GH, Hone J, Heinz TF, Shan J (2013) Tightly bound trions in monolayer MoS<sub>2</sub>. *Nat Mater* 12(3):207–211
38. Liu BL, Fathi M, Chen L, Abbas A, Ma YQ, Zhou CW (2015) Chemical vapor deposition growth of monolayer WSe<sub>2</sub> with tunable device characteristics and growth mechanism study. *ACS Nano* 9(6):6119–6127
39. Lan C, Zhou Z, Wei R, Ho JC (2019) Two-dimensional perovskite materials: from synthesis to energy-related applications. *Materials today energy* 11:61–82
40. Wang K, Huang B, Tian M, Ceballos F, Lin MW, Mahjouri-Samani M, Boulesbaa A, Puzetky AA, Rouleau CM, Yoon M, Zhao H, Xiao K, Duscher G, Geoghegan DB (2016) Interlayer coupling in twisted WSe<sub>2</sub>/WS<sub>2</sub> bilayer heterostructures revealed by optical spectroscopy. *ACS Nano* 10(7):6612–6622
41. Tonndorf P, Schmidt R, Bottger P, Zhang X, Borner J, Liebig A, Albrecht M, Kloc C, Gordan O, Zahn DRT, de Vasconcelos SM, Bratschkitsch R (2013) Photoluminescence emission and Raman response of monolayer MoS<sub>2</sub>, MoSe<sub>2</sub>, and WSe<sub>2</sub>. *Opt Express* 21(4):4908–4916
42. Cai ZY, Liu BL, Zou XL, Cheng HM (2018) Chemical vapor deposition growth and applications of two-dimensional materials and their heterostructures. *Chem Rev* 118(13):6091–6133
43. Desai SB, Seol G, Kang JS, Fang H, Battaglia C, Kapadia R, Ager JW, Guo J, Javey A (2014) Strain-induced indirect to direct bandgap transition in multi layer WSe<sub>2</sub>. *Nano Lett* 14(8):4592–4597
44. Wang YL, Cong CX, Qiu CY, Yu T (2013) Raman spectroscopy study of lattice vibration and crystallographic orientation of monolayer MoS<sub>2</sub> under uniaxial strain. *Small* 9(17):2857–2861
45. Zhou HL, Wang C, Shaw JC, Cheng R, Chen Y, Huang XQ, Liu Y, Weiss NO, Lin ZY, Huang Y, Duan XF (2015) Large area growth and electrical properties of p-type WSe<sub>2</sub> atomic layers. *Nano Lett* 15(1):709–713
46. Cong CX, Shang JZ, Wu X, Cao BC, Peimyo N, Qiu C, Sun LT, Yu T (2014) Synthesis and optical properties of large-area single-crystalline 2D semiconductor WS<sub>2</sub> monolayer from chemical vapor deposition. *Adv Opt Mater* 2(2):131–136
47. Li HA, Li Y, Aljarb A, Shi YM, Li LJ (2018) Epitaxial growth of two-dimensional layered transition-metal dichalcogenides: growth mechanism, controllability, and scalability. *Chem Rev* 118(13):6134–6150
48. Cain JD, Shi FY, Wu JS, Dravid VP (2016) Growth mechanism of transition metal dichalcogenide monolayers: the role of self-seeding fullerene nuclei. *ACS Nano* 10(5):5440–5445
49. Ouyang F, Yang Z, Xiang N, Wu N, Yu C, Xiang X (2014) Hydrogenation-induced edge magnetization in armchair MoS<sub>2</sub> nanoribbon and electric field effects. *Appl Phys Lett* 104(7):699
50. Wang Z, Dong Z, Zhu H, Jin L, Chiu M-H, Li L-J, Xu Q-H, Eda G, Maier SA, Wee ATS, Qiu C-W, Yang JKW (2018) Selectively plasmon-enhanced second-harmonic generation from monolayer tungsten diselenide on flexible substrates. *ACS Nano* 12(2):1859–1867
51. Zhao S, Tao L, Miao P, Wang X, Liu Z, Wang Y, Li B, Sui Y, Wang Y (2018) Strong room-temperature emission from defect states in CVD-grown WSe<sub>2</sub> nanosheets. *Nano Res* 11(7):3922–3930
52. Li TS, Li ML, Lin Y, Cai HB, Wu YM, Ding HY, Zhao SW, Pan N, Wang XP (2018) Probing exciton complexes and charge distribution in ink-slab-like WSe<sub>2</sub> homojunction. *ACS Nano* 12(5):4959–4967
53. Ahn S, Kim G, Nayak PK, Yoon SI, Lim H, Shin HJ, Shin HS (2016) Prevention of transition metal dichalcogenide photodegradation by encapsulation with h-BN layers. *ACS Nano* 10(9):8973–8979
54. Chow PK, Jacobs-Gedrim RB, Gao J, Lu TM, Yu B, Terrones H, Koratkar N (2015) Defect-induced photoluminescence in monolayer semiconducting transition metal dichalcogenides. *ACS Nano* 9(2):1520–1527
55. Wu Z, Zhao W, Jiang J, Zheng T, You Y, Lu J, Ni Z (2017) Defect activated photoluminescence in WSe<sub>2</sub> monolayer. *J Phys Chem C* 121(22):12294–12299

56. Nan HY, Wang ZL, Wang WH, Liang Z, Lu Y, Chen Q, He DW, Tan PH, Miao F, Wang XR, Wang JL, Ni ZH (2014) Strong photoluminescence enhancement of MoS<sub>2</sub> through defect engineering and oxygen bonding. *ACS Nano* 8(6):5738–5745
57. Kang WT, Lee IM, Yun SJ, Song YI, Kim K, Kim DH, Shin YS, Lee K, Heo J, Kim YM (2018) Direct growth of doping controlled monolayer WSe<sub>2</sub> by selenium-phosphorus substitution. *Nanoscale* 10(24):11397–11402
58. Kim MS, Yun SJ, Lee Y, Seo C, Han GH, Kim KK, Lee YH, Kim J (2016) Biexciton emission from edges and grain boundaries of triangular WS<sub>2</sub> monolayers. *ACS Nano* 10(2):2399–2405
59. Kim H, Ahn GH, Cho J, Amani M, Mastandrea JP, Groschner CK, Lien D-H, Zhao Y, Ager JW, Scott MC, Chrzan DC, Javey A (2019) Synthetic WSe<sub>2</sub> monolayers with high photoluminescence quantum yield. *Sci Adv* 5(1):eaau4728
60. Wang Z, Dong ZG, Gu YH, Chang YH, Zhang L, Li LJ, Zhao WJ, Eda G, Zhang WJ, Grinblat G, Maier SA, Yang JKW, Qiu CW, Wee ATS (2016) Giant photoluminescence enhancement in tungsten-diselenide-gold plasmonic hybrid structures. *Nat Commun* 7:11283
61. Bacher G, Schweizer H, Kovac J, Forchel A, Nickel H, Schlapp W, Lösch R (1991) Influence of barrier height on carrier dynamics in strained In<sub>x</sub>Ga<sub>1-x</sub>As/GaAs quantum wells. *Phys Rev B* 43(11):9312–9315
62. Zhou JD, Lin JH, Huang XW, Zhou Y, Chen Y, Xia J, Wang H, Xie Y, Yu HM, Lei JC, Wu D, Liu FC, Fu QD, Zeng QS, Hsu CH, Yang CL, Lu L, Yu T, Shen ZX, Lin H, Yakobson BI, Liu Q, Suenaga K, Liu GT, Liu Z (2018) A library of atomically thin metal chalcogenides. *Nature* 556(7701):355–359
63. Gong YJ, Ye GL, Lei SD, Shi G, He YM, Lin JH, Zhang X, Vajtai R, Pantelides ST, Zhou W, Li B, Ajayan PM (2016) Synthesis of millimeter-scale transition metal dichalcogenides single crystals. *Adv Funct Mater* 26(12):2009–2015
64. Cai L, Shearer MJ, Zhao Y, Hu Z, Wang F, Zhang Y, Eliceiri KW, Hamers RJ, Yan W, Wei S, Tang M, Jin S (2018) Chemically derived kirigami of WSe<sub>2</sub>. *J Am Chem Soc* 140(35):10980–10987
65. Najmaei S, Ajayan PM, Lou J (2013) Quantitative analysis of the temperature dependency in Raman active vibrational modes of molybdenum disulfide atomic layers. *Nanoscale* 5(20):9758–9763

## Publisher's Note

Springer Nature remains neutral with regard to jurisdictional claims in published maps and institutional affiliations.

Submit your manuscript to a SpringerOpen<sup>®</sup> journal and benefit from:

- Convenient online submission
- Rigorous peer review
- Open access: articles freely available online
- High visibility within the field
- Retaining the copyright to your article

---

Submit your next manuscript at ► [springeropen.com](https://www.springeropen.com)

---